Nonlinear Color–Metallicity Relations of Globular Clusters. VI. On Calcium II Triplet Based Metallicities of Globular Clusters in Early-type Galaxies

Chul Chung[1], Suk-Jin Yoon[1,2], Sang-Yoon Lee[1,2], and Young-Wook Lee[1,2]

Department of Astronomy & Center for Galaxy Evolution Research, Yonsei University, Seoul 120-749, Republic of Korea

sjyoon@galaxy.yonsei.ac.kr

ABSTRACT

The metallicity distribution function of globular clusters (GCs) in galaxies is a key to understanding galactic formation and evolution. The calcium II triplet (CaT) index has recently become a popular metal abundance indicator thanks to its sensitivity to GC metallicity. Here we revisit and assess the reliability of CaT as a metallicity indicator using our new stellar population synthesis simulations based on empirical, high-resolution fluxes. The model shows that the CaT strength of old (> 10 Gyr) GCs is proportional to [Fe/H] below -0.5. In the modest metal-rich regime, however, CaT does not increase anymore with [Fe/H] due to the little contribution from coolest red giant stars to the CaT absorption. The nonlinear nature of the color–CaT relation is confirmed by the observations of GCs in nearby early-type galaxies. This indicates that the CaT should be used carefully when deriving metallicities of metal-rich stellar populations. Our results offer an explanation for the observed sharp difference between the color and CaT distributions of GCs in the same galaxies. We take this as an analogy to the view that metallicity–color and metallicity–Lick index nonlinearity of GCs is primarily responsible for their observed "bimodal" distributions of colors and absorption indices.

Subject headings: globular clusters: general — stars: abundances — stars: evolution — stars: horizontal-branch

[1] Center for Galaxy Evolution Research, Yonsei University, Seoul 120-749, Republic of Korea; sjyoon@galaxy.yonsei.ac.kr.

[2] Department of Astronomy, Yonsei University, Seoul 120-749, Republic of Korea; sjyoon@galaxy.yonsei.ac.kr.

1. INTRODUCTION

Deriving metallicity of globular clusters (GCs) in early-type galaxies (ETGs) has always been an important issue since the discovery of bimodal color distributions of GC systems in ETGs. Colors are direct proxies for metallicity of old-aged stellar populations, and thus color bimodality was interpreted as the bimodal metallicity distributions (e.g., Harris 1991; West et al. 2004; Brodie & Strader 2006). However, after Yoon et al. (2006, Paper I) claimed that the conversion between color and metallicity is nonlinear due mainly to the effect of hot horizontal-branch (HB) stars on the integrated colors, our subsequent studies (Yoon et al. 2011a, Paper II; Yoon et al. 2013, Paper IV) supported nonlinear color–metallicity relations (CMRs) based on the multiband photometry of GC color distributions of M87 and M84. Yoon et al. (2011b, Paper III) further derived unimodal metallicity distribution functions of external GC systems which are similar to those of halo field stars of their host galaxies. In order to derive more accurate metallicity of GCs in ETGs, various spectroscopic observations have been performed (Peng et al. 2004; Strader et al. 2005; Cenarro et al. 2007; Beasley et al. 2008; Woodley et al. 2010; Foster et al. 2011; Park et al. 2012a,b; Chies-Santos et al. 2012), but, as confirmed in Chung et al. (2013a), Kim et al. (2013, Paper V, M31 spheroidal component GCs), and Kim et al. (2015, Paper VII, NGC 5128 GCs), the index–metallicity relations (IMRs) are also not free from the effect of hot HB stars.

Recently, calcium II triplet (CaT) has been getting attention in the determination of metallicity of GCs in ETGs (Foster et al. 2010, 2011; Usher et al. 2012, 2013, 2015; Brodie et al. 2012) because, compared to its sensitivity to metallicity, it is relatively less sensitive to hot stars such as blue HB stars in simple stellar populations (SSPs). CaT is one of the strongest absorption features in the near infrared (8498, 8542, and 8662 Å) and very sensitive to metallicity and surface gravity of stars (Cenarro et al. 2001a,b, 2002). Therefore, CaT has been widely used as a metallicity indicator of various stellar systems such as GCs and open clusters in the Milky Way (MW), and extragalactic GCs, as well as dwarf galaxies (e.g., Armandroff & Zinn 1988; Carrera 2012; Foster et al. 2010; Battaglia et al. 2008). However, as shown in the CaT models of Vazdekis et al. (2003), when the metallicity is high enough as $[M/H] \geq -0.5$, the CaT is not sensitive to the metallicity anymore, rather sensitive to the slope of initial mass functions of stellar populations. Thus, probing the validity of using the CaT as a direct metallicity indicator is one of the most important issues. In this paper we present the CaT model for SSPs based on empirical SEDs, and attempt to test whether CaT is a reliable metallicity tracer or not. Section 2 gives the construction of our CaT SSP model. In section 3, we present CaT definitions adopted in this paper and results of our CaT models. Section 4 compares our models with GCs in various ETGs. Section 5 discusses the implications of the nonlinear CaT–metallicity relation on the CaT distributions of GCs.

2. CONSTRUCTION OF MODELS

The CaT model presented in this paper has been constructed following the standard Yonsei evolutionary population synthesis (YEPS) model described in Chung et al. (2013a,b). The model is an extended version of our previous models to include the near infrared wavelengths. The only difference is that instead of adopting BaSel 3.1 library (Westera et al. 2002), we have adopted empirical, high-resolution SEDs. The input parameters, such as the initial mass function of main-sequence stars, the mass dispersion of HB stars, the mass-loss efficiency along the giant branch stars, and the age of inner-halo GCs in the MW, are exactly the same as in Table 1 of Chung et al. (2013a).

The empirical spectra we have adopted in the model are the Cenarro (Cenarro et al. 2001a,b, 2002) and the INDO-US spectral libraries (Valdes et al. 2004) to cover the near infrared wavelength regime. The Cenarro library comprises spectra of 702 stars with the wavelength coverage running from 8348 to 9020 Å with a resolution of 1.5 Å. The INDO-US library contains spectra of 1273 stars with the wavelength from 3460 to 9464 Å with 1 Å spectral resolution, but some of spectra have several wavelength intervals. Of 702 and 1273 empirical spectra of the Cenarro and INDO-US, we have selected 602 and 694 spectra, respectively, that have well determined stellar parameters and fully cover the CaT absorption features without any spectral gaps. We have transformed stellar parameters (i.e., effective temperature, gravity, and total metallicity) of the INDO-US library to those of the Cenarro library using the transform equations from INDO-US to MILES library of Vazdekis et al. (2012). Since the Cenarro and MILES (Sánchez-Blázquez et al. 2006) share 369 stars in common and they show almost the same stellar parameters (Cenarro et al. 2007), the stellar parameter transformation from INDO-US to MILES library is equivalent to the transformation from INDO-US to Cenarro library.

In order to incorporate empirical SEDs in our model, we need to calibrate fluxes of the two libraries. We firstly design box-shaped filter ranging from 8610 to 8810 Å because of the Cenarro spectra covering wavelengths from 8350 to 9150 Å. Secondly, we derive magnitudes of empirical spectra within the filter. At the same time, using the same filter we derive the magnitude of BaSel 3.1 spectrum at a given stellar parameter. After that we compare every empirical spectrum with the theoretical spectrum and calibrate the continuum levels of empirical spectra in units of [erg s^{-1}cm^{-2}Å^{-1}]. In this process we do not mix two libraries together, and we separately develop two models based on two libraries. Therefore, the effect of missing spectral range on broadband colors reported in Vazdekis et al. (2012) is negligible in our models because we deal with narrow wavelength region of CaT within a given spectral library. We apply these calibrated empirical SEDs to stars in our synthetic color–magnitude diagram described in Chung et al. (2013a) and reproduce empirical SSP models for CaT.

In this paper, we choose to use the total metallicity [Z/H] for the construction of our models. Therefore, the CaT models for the enhanced α-elements are mimicked by increasing the total metallicity [Z/H]. The enhancement of α-elements is assumed to be [α/Fe] = 0.3 (Woodley et al.

2010; Chies-Santos et al. 2012), and all models are constructed using α-elements enhanced Y^2-stellar evolutionary tracks (Kim et al. 2002). We assume that [Z/H] relates to [Fe/H] with the relations of [Z/H] = [Fe/H] + 0.723 × [α/Fe] for [a/Fe] = 0.3 (see also, Thomas et al. 2003; Lee & Worthey 2005; Vazdekis et al. 2015). The constant 0.723 is derived from the α-elements enhancement patterns of Y^2-isochrones with [α/Fe] = 0.3 which show 2 times enhancement in O, Ne, Na, Mg, Si, P, S, Cl, Ar, Ca, and Ti, and depletion in Al and Mn (see Table 2 of Chung et al. 2013a). We apply this relation to derive [Z/H] of all empirical stars, and construct CaT SSP models for [α/Fe] = 0.3.

3. MEASUREMENT OF CaT AND MODEL RESULTS

There exist several index definitions of CaT when measuring its strength from observations (Jones et al. 1984; Bica & Alloin 1987; Armandroff & Zinn 1988; Diaz et al. 1989; Zhou 1991; Delisle & Hardy 1992; Rutledge et al. 1997; Cenarro et al. 2001a; Foster et al. 2010). Among these, we have chosen the definition of Cenarro et al.'s (2001a, C01) and Foster et al.'s (2010, F10). The upper row of Figure 1 shows the chosen CaT definitions along with our synthetic model spectra. The definition of C01 is designed for measuring the integrated CaT of galaxies and less affected by adjacent spectral features, such as Paschen and Fe I absorptions. In order to compare our model with GC observations of F10 and Usher et al. (2012), we have adopted the method of F10 which measures the value of CaT from the normalized spectra whose continua are set to unity. F10 only measured the absorption features of central passbands ([8490.0–8506.0], [8532.0–8552.0], and [8653.0–8672.0]) of Armandroff & Zinn (1988) and did not consider continuum passbands of each index. Narrowing index passbands and setting continua as unity can also reduce the contamination of other adjacent absorption features (Foster et al. 2010). We have followed the same way of the fitting and normalization of model spectra proposed in F10 by using the IRAF CONTINUUM routine with Chebyshev polynomials of the order of eight. Before we measure CaT values, we apply Gaussian kernel smoothing to our model spectra based on Cenarro and INDO-US library in order to reduce the resolution of our model spectra to that of the Lick system. We will use the CaT index whose value was measured using the scheme of F10 and C01 as "CaT_{F10}" and "CaT_{C01}", respectively, in what follows.

The bottom row of Figure 1 provides the relations among CaT_{C01}, CaT_{F10}, and CaT_{AZ88} (the classical index definition of Armandroff & Zinn 1988). The indices were measured from our 13-Gyr model SEDs and the 12.5893-Gyr SED of Vazdekis et al. (2003). The measurement of CaT_{F10} only is taken from fitted spectra as shown in the top right panel. For the conversion between our CaT measurement and the other systems, we provide the best fitting relations in the following Equations 1 (for the red line in the bottom row of Figure 1) and 2 (for the blue line in the bottom row of Figure 1).

$$CaT_{AZ88} = 0.7637 \times CaT_{C01} + 0.5925 \tag{1}$$

$$CaT_{\mathrm{AZ88}} = 0.9026 \times CaT_{\mathrm{F10}} + 0.3436 \qquad (2)$$

The CaT models based on the Cenarro and INDO-US libraries are given in Figure 2. Our 3-, 5-, 10-, 12-, and 14-Gyr model predictions for CaT based on two empirical libraries are given in Table 1. Our simple stellar population models for CaT cover age ranging from 3 to 15 Gyr, metallicity from [Fe/H] = −2.5 to 0.5, and scaled-solar abundance mixture and [α/Fe] = 0.3. The entire data are available at http://web.yonsei.ac.kr/cosmic/data/YEPS.htm.

The CaT–[Fe/H] relation for old age models (≥ 10 Gyr) shows an one-to-one correlation below [Fe/H] = −0.5. In the higher metallicity regime ([Fe/H] ≥ −0.5), however, CaT does not trace [Fe/H] remaining constant around 8 Å for CaT_{C01} and 7 Å for CaT_{F10}. As a result, the overall shape of the relations is characterized by being nonlinear. In order to find the physical cause for such nonlinearity, we first have checked whether hot HB stars affect the CaT strength as does for the optical colors (Paper I; Paper II; Paper III; Paper IV) and spectral indices (Chung et al. 2013a; Paper V; Paper VII). The age of models in the upper row of Figure 2 is 12 Gyr, and the stellar populations at this age produce hot blue HB stars below [Fe/H] ∼ −1.5 (Chung et al. 2013a). As shown in the Figure, the effect of hot HB stars (> 10,000 K) on CaT is almost negligible for both CaT_{C01} and CaT_{F10}. This is caused by insensitivity of CaT to hot stars (Cenarro et al. 2002) and by the small flux contribution of hot HB stars in the near infrared regime. Our model shows that the flux contribution of HB stars to the total flux at 8700 Å is only ∼5 %, when the age and metallicity of SSP is 12 Gyr and [Fe/H] = −1.5. The effect of cool red HB stars on CaT is a bit stronger than that of hot blue HB stars because the low gravity (log g ≤ 2.5) and low temperature (T_{eff} ∼ 5000 K) of those stars increase the strength of CaT (Cenarro et al. 2002). For instance, cool HB stars from metal-rich ([Fe/H] = 0.5) stellar populations increase CaT by up to 0.5 Å. This is however not enough to explain the cause of the nonlinear CaT–metallicity relation.

In the bottom row of Figure 2 we have tested the effect of age on CaT. If the age of stellar population is greater than 10 Gyr, the model IMRs do not change significantly with age. However, the CaT models of 3 Gyr show slightly different IMRs compared to the old age IMRs. In the metal-poor regime, the younger age model shows enhanced CaT due to the effect of hot turn-off stars that heavily contaminate Ca II by increasing the Paschen lines (Cenarro et al. 2002).

Figure 3 provides an explanation for nonlinearity of the CaT IMR. In general, CaT is sensitive to metallicity and gravity of stars (Rutledge et al. 1997; Warren & Cole 2009; Vasquez et al. 2015). These typical characteristics however are only for the stars whose temperature is between T_{eff} ∼ 3870 and 7200 K. As shown in the left panel of Figure 3, when the temperature of stars is cooler than T_{eff} ∼ 3870 K (grey dashed vertical lines in Figure 3), the strength of CaT gradually decreases with decreasing T_{eff} regardless of metallicity and gravity of stars. The reason for this is that the formation of calcium II ionized absorption lines becomes less efficient in the lower temperature because calcium goes into a neutral state (Cenarro et al. 2002). As a result, if cool stars are dominant in a SSP, the strength of CaT can not be the indicator of metallicity and gravity of

stellar populations. The right panel of Figure 3 shows that most of RGB stars whose [Fe/H] are greater than –0.89 are populated in the low temperature ($T_{eff} < 3870$ K) regime. This explains why the strength of CaT for SSPs does not increase with increasing metallicity, converging to the same equivalent width (EW) around 8 Å and 7 Å for CaT_{C01} and CaT_{F10}, respectively. We note that the similar CaT–metallicity relation is also found in the model of Vazdekis et al. (2003, in their Table 3).

In order to explain the offsets between Cenarro and INDO-US library, Figure 4 compares the CaT values of common stars in both libraries measured in C01 and F10 definition. We note that F10 definition is relatively less affected by the flux calibration due to its flux normalization process before measuring CaT value. Although we use two different definitions of CaT, the CaT values measured in INDO-US library show, on average, 0.37 and 0.51 Å enhanced CaT in C01 and F10 definitions, respectively. We speculate that this is due to the intrinsic difference (such as inhomogeneous observations and different flux calibrations) between empirical libraries and this is why the model based on INDO-US library shows ∼1 Å offset from the model based on Cenarro library.

It is well established that there exists the well-known α-element bias with respect to the metallicity of stars in the empirical libraries (e.g., Sansom et al. 2013; Vazdekis et al. 2015). In Figure 5, we present [α/Fe] = 0.0 model for CaT, which adopts scaled-solar stellar evolutionary tracks. In general, the scaled-solar model shows slightly enhanced CaT strength compared to that of α-elements enhanced models. If scaled-solar abundance for metal-rich populations ([Fe/H] > -0.5) is assumed, our models show, on average, 0.6 Å enhanced CaT, but the saturation of CaT in the metal-rich regime still exists.

4. COMPARISON WITH OBSERVATIONS

Figure 6 shows the CaT versus $(g-i)_0$ diagram of 901 GCs in 11 ETGs in Usher et al. (2012) as part of the SAGES Legacy Unifying Globulars and Galaxies Survey[1]. We have denoted CaT of Usher et al. (2012) as CaT_{F10} as they followed the CaT measurement of F10. One can expect a linear correlation between CaT_{F10} and $(g-i)_0$ if both are direct metallicity tracers. However, the observed relation is nonlinear steepening above $CaT_{F10} \sim 6.5$ Å and $(g-i) \sim 0.9$ mag. This implies that at least one of two metallicity indicators is not directly tracing the metallicity of stellar populations. Although the $(g-i)_0$–metallicity relation is inflected (Paper I; Paper II; Paper IV), the $(g-i)_0$ color is just proportional to metallicity. However, as shown in Figure 1, our new IMR of CaT does not increase with increasing metallicity in the metal-rich regime. This gives rise to the broken linear relation with different slopes below and above the point at $(g-i)_0 \sim 0.9$.

We overplot our models in the right panel of Figure 6. The hot HB stars associated with

---

[1]http://sluggs.swin.edu.au

metal-poor, old stellar populations make a "wavy" feature in the CaT–$(g-i)_0$ relation, but this effect disappears in the metal-rich regime. Regardless of the choice of empirical libraries, our models show a converging feature around $CaT_{\rm F10} \sim 7$ Å because of the low formation efficiency of CaT for the most metal-rich stars. As a consequence, the overall shapes of our old age models (≥ 10 Gyr) show reasonably good agreement with the observation.

We compare our models with GCs of individual galaxies in Figure 7. Our models show a good fit to most of GCs with small observational errors. The GCs in NGC 1407, NGC 4278, and NGC 4365 well follow old age models. The GCs of NGC 3115 show a clear separation between metal-poor and rich GCs, yet GCs still lie along with our models. As suggested by Cantiello et al. (2014), several metal-rich GCs in NGC 3115 prefer the younger age model (cyan lines), and this explains the presence of a group of metal-rich GCs with small offsets from models. In the same vein, the metal-rich GCs in NGC 4494 can be also explained by younger age stellar populations (Foster et al. 2011). The GC system in NGC 3377 does not have enough metal-rich GCs but in the metal-poor regime it agrees our models well. The GCs in NGC 5846, NGC 2768, NGC 1400, NGC 821, and NGC 7457 are located along with our old age model predictions, although they have the small GC numbers. The CaT of GCs in NGC 1407 and the MW by F10 is plotted in the rightmost bottom panel. They also show good agreement with our models in the $(B-I)_0$ and CaT plane.

5. DISCUSSION

We have presented the CaT model for SSPs based on the high-resolution empirical SEDs. We have demonstrated that the well-known metallicity indicator CaT loses its sensitivity to metallicity in the metal-rich regime, showing the highly nonlinear CaT–metallicity relation. Our model shows a good agreement with the observed GCs in the MW and ETGs. If the underlying IMR of GC CaT is linear, this agreement between our model and the observation is hard to be explained. Most studies however have adopted the linear one-to-one correlation for the conversion of CaT to metallicity (e.g., Foster et al. 2010, 2011; Brodie et al. 2012; Usher et al. 2012, 2013).

An implication of the nonlinear IMR of CaT lies in the CaT distribution of GCs in ETGs. As Paper I, Paper II, and Paper IV showed the case of optical colors, the nonlinear CaT–metallicity relation is most likely to reproduce the observed CaT distributions of GCs in ETGs from a single-peaked, broad metallicity distribution function (MDF). Figures 8 and 9 show the simulations for GC samples of Usher et al. (2012) and F10 using our CaT–metallicity and color–metallicity relations. We simulate the color distributions of GCs and find the best Gaussian MDFs for the observed distributions. Then we simply apply those Gaussian MDFs to our empirical CaT–metallicity relations reproducing the CaT distributions. The number of model GCs for the Gaussian MDF is 10^6, and the observational uncertainties are taken into account in the projected CaT, $(g-i)_0$, and $(B-I)_0$ distributions. Based on the observed GCs and 10^4 randomly selected model GCs, we perform the Gaussian Mixture Modeling (GMM) analysis (Muratov & Gnedin 2010). Table 2

summarizes the result for Figures 8 and 9.

In the top panel of Figure 8, we perform the projection simulation for all 901 GCs of Usher et al. (2012). The shapes of the observed $(g - i)_0$ distributions of 901 GCs are well reproduced by our model, when the GC MDF is assumed to be $\langle[\text{Fe/H}]\rangle = -0.80$ with $\sigma_{[\text{Fe/H}]} = 0.55$ and the age of the SSP is some 13 Gyr. The GMM analysis for the $(g - i)_0$ observation gives the peaks at 0.812 and 1.051 mag with the number fraction of 39.67 and 60.33 %, respectively. The simulated $(g-i)_0$ distribution shows similar two peaks at 0.802 and 1.071 mag with the fraction of 31.10 and 68.90 %, respectively. The observed CaT distribution shows the metal-rich peak at 7.293 Å and the metal-poor bump at 5.087 Å with the fraction of 34.28 and 65.72 %, respectively. The same MDF produces a bimodal CaT histogram with at 5.224 and 6.704 Å with the fraction of 53.25 and 46.75 %, respectively, based on the Cenarro IMR. The prominent metal-rich peaks can be explained by the nonlinear IMR of CaT that makes metal-rich GCs pile up at $CaT \sim 6.7$ Å. Slight offsets between the observed and simulated CaT distribution may be attributed to the incompleteness of the population synthesis model in terms of stellar evolutionary tracks and/or empirical SEDs.

In the second row of Figure 8, we present histograms for 779 GCs without NGC 3115 GCs. NGC 3115 are well known for hosting two metallicity groups of GCs (Arnold et al. 2011; Brodie et al. 2012; Cantiello et al. 2014; Jennings et al. 2014). To see the pure effect of the nonlinear CaT–metallicity relation on the CaT distribution, we take out 122 GCs in NGC 3115 which may potentially mislead the analysis of the morphology of GC distributions. A slightly smaller MDF dispersion with the same mean metallicity ($\sigma_{[\text{Fe/H}]} = 0.50$ and $\langle[\text{Fe/H}]\rangle = -0.80$) reproduces both the $(g-i)_0$ and CaT_{F10} histograms, simultaneously. A GMM bimodal fitting for $(g-i)_0$ yields 0.817 and 1.041 mag with 37.01 and 62.99 % number fraction, respectively, for the observed histogram, and 0.806 and 1.064 mag with 30.38 and 69.62 % number fraction, respectively, for the simulated one. The exclusion of NGC 3115 GCs from all GC sample makes the observed metal-poor peak in the CaT histogram of GCs slightly weaker. Our model reproduces this observation well. A GMM bimodal fitting for CaT_{F10} gives 4.686 and 7.090 Å peaks with 27.13 and 72.87 % number fraction, respectively, for the observed histogram, and 6.076 and 7.877 Å peaks with 38.07 and 61.93 % number fraction, respectively, for the simulated one based on the INDO-US IMR.

We also perform the projection simulations for GC systems of individual ETGs. Middle and bottom rows in Figure 8 show the large ETG NGC 1407 observed by Usher et al. (2012) and F10. F10 observed CaT of 144 GCs in NGC 1407, and Usher et al. (2012) added more GCs and remeasured CaT for all GCs. The observation by F10 shows that only the $(B - I)_0$ distribution has bimodality but the CaT distribution prefers skewed Gaussian distribution. Our projection test based on 13 Gyr relations reproduces simultaneously both the CaT and $(B - I)_0$ observations of F10 using the Gaussian MDF of $\langle[\text{Fe/H}]\rangle = -0.80$ with $\sigma_{[\text{Fe/H}]} = 0.55$. On the other hand, the GCs of Usher et al. (2012) show bimodality for both the $(g - i)_0$ and CaT distributions. Our models for NGC 1407 show bimodal distributions both in $(g - i)_0$ and CaT. However, the metal-poor bump (at $CaT_{\text{F10}} \sim 4.8$Å) in the CaT distribution is not reproduced. The parameters for these distributions analyzed by the GMM test are listed in Table 2.

In Figure 9, the simulated distributions for the GC systems in NGC 4278, NGC 4365, and NGC 3377 concur with the observations (see Table 2). A small metal-rich bump (at $CaT_{\rm F10} \sim 7.5$Å) in the CaT distribution of NGC 4365 GCs seems related to the intermediate age GC populations reported by Larsen et al. (2003, 2005) and Blom et al. (2012). Our simulation is not successful in reproducing the distributions of NGC 3115 GC system. Strongly separated two peaks in $(g-i)_0$ is hard to be reproduced under the assumption of a single Gaussian MDF. As suggested by Brodie et al. (2012) and Cantiello et al. (2014), this is because NGC 3115 has two metallicity groups of GCs confirmed by optical–to–NIR colors. The detection of metal-poor stellar halo in NGC 3115 also provides a good explanation for two separate GC groups (Peacock et al. 2015). Except for NGC 3115, our model reproduces the $(g-i)_0$ and CaT distributions *simultaneously* based on the $(g-i)_0$ CMR and CaT IMR that are nonlinear.

Based on our CaT IMR and $(g-i)_0$ CMR, we have derived GC MDFs from CaT and $(g-i)_0$ of 779 GCs. Figure 10 shows the result of the inverse projection and compares the derived GC MDFs with that presented in Usher et al. (2012). We exclude GCs of NGC 3115 in this simulation for reasons mentioned above. For the conversion of [Fe/H]$_{\rm Usher}$ from $(g-i)_0$, we adopt Eq. 10 of Usher et al. (2012). Both MDFs derived from our CaT and $(g-i)_0$ models show similar skewed Gaussian shapes with a single peak around [Fe/H] ~ -1.0. These shapes are consistent with the typical MDFs of field stars in ETGs (Paper III). Note that the MDFs from our CaT model have small peaks where [Fe/H] ≥ 0.2. These peaks are caused by the saturated features in CaT IMRs that make hard to determine the metallicity of metal-rich stellar populations. The right panel, on the other hand, shows that the MDF derived from CaT has two peaks at [Fe/H] $= -1.41$ and -0.43 and the MDF from $(g-i)_0$ at [Fe/H] $= -1.10$ and -0.37 based on the GMM test. The two metallicity groups have different ratio between metal-poor and metal-rich GCs with 34.0 : 66.0% and 47.1 : 52.9%, respectively.

The nonlinearity of the CaT IMR also have an important implication on the integrated CaT of various stellar systems. As shown in our models, if cool stars are dominant in a given stellar system, the integrated CaT can not be the indicator of metallicity or even the calcium abundance. We speculate that this is why calcium abundance derived from calcium II lines is unexpectedly low in various stellar systems. For example, the observed CaT (Saglia et al. 2002) and CaHK (Worthey et al. 2011) of ETGs suggest constant or even decreasing calcium abundances with increasing mass of galaxies. These results go against with the general trend of mass–metallicity relation for ETGs. However, a larger fraction of cool metal-rich stars in the more massive ETGs could explain the observed CaT feature of ETGs. We will fully discuss the issue in our forthcoming paper.

REFERENCES

Arnold, J. A., Romanowsky, A. J., Brodie, J. P., et al. 2011, ApJ, 736, L26

Armandroff, T. E., & Zinn, R. 1988, AJ, 96, 92

Battaglia, G., Irwin, M., Tolstoy, E., et al. 2008, MNRAS, 383, 183

Beasley, M. A., Bridges, T., Peng, E., et al. 2008, MNRAS, 386, 1443

Bica, E., & Alloin, D. 1987, A&A, 186, 49

Blom, C., Spitler, L. R., & Forbes, D. A. 2012, MNRAS, 420, 37

Brodie, J. P., & Strader, J. 2006, ARA&A, 44, 193

Brodie, J. P., Usher, C., Conroy, C., et al. 2012, ApJ, 759, L33

Cantiello, M., Blakeslee, J. P., Raimondo, G., et al. 2014, A&A, 564, LL3

Carrera, R. 2012, A&A, 544, A109

Cenarro, A. J., Beasley, M. A., Strader, J., Brodie, J. P., & Forbes, D. A. 2007, AJ, 134, 391

Cenarro, A. J., Cardiel, N., Gorgas, J., et al. 2001, MNRAS, 326, 959

Cenarro, A. J., Gorgas, J., Cardiel, N., et al. 2001, MNRAS, 326, 981

Cenarro, A. J., Gorgas, J., Cardiel, N., Vazdekis, A., & Peletier, R. F. 2002, MNRAS, 329, 863

Cenarro, A. J., Peletier, R. F., Sánchez-Blázquez, P., et al. 2007, MNRAS, 374, 664

Chies-Santos, A. L., Larsen, S. S., & Kissler-Patig, M. 2012, MNRAS, 427, 2349

Chung, C., Lee, S.-Y., Yoon, S.-J., & Lee, Y.-W. 2013, ApJ, 769, L3

Chung, C., Yoon, S.-J., Lee, S.-Y., & Lee, Y.-W. 2013, ApJS, 204, 3

Delisle, S., & Hardy, E. 1992, AJ, 103, 711

Diaz, A. I., Terlevich, E., & Terlevich, R. 1989, MNRAS, 239, 325

Foster, C., Forbes, D. A., Proctor, R. N., et al. 2010, AJ, 139, 1566

Foster, C., Spitler, L. R., Romanowsky, A. J., et al. 2011, MNRAS, 415, 3393

Harris, W. E. 1991, ARA&A, 29, 543

Jennings, Z. G., Strader, J., Romanowsky, A. J., et al. 2014, AJ, 148, 32

Jones, J. E., Alloin, D. M., & Jones, B. J. T. 1984, ApJ, 283, 457

Kim, S., Yoon, S.-J., Chung, C., et al. 2013, ApJ, 768, 138

Kim, Y.-C., Demarque, P., Yi, S. K., & Alexander, D. R. 2002, ApJS, 143, 499

Larsen, S. S., Brodie, J. P., Beasley, M. A., et al. 2003, ApJ, 585, 767

Larsen, S. S., Brodie, J. P., & Strader, J. 2005, A&A, 443, 413

Lee, H.-c., & Worthey, G. 2005, ApJS, 160, 176

Muratov, A. L., & Gnedin, O. Y. 2010, ApJ, 718, 1266

Park, H. S., Lee, M. G., Hwang, H. S., et al. 2012, ApJ, 759, 116

Park, H. S., Lee, M. G., & Hwang, H. S. 2012, ApJ, 757, 184

Peng, E. W., Ford, H. C., & Freeman, K. C. 2004, ApJ, 602, 705

Peacock, M. B., Strader, J., Romanowsky, A. J., & Brodie, J. P. 2015, ApJ, 800, 13

Rutledge, G. A., Hesser, J. E., Stetson, P. B., et al. 1997, PASP, 109, 883

Saglia, R. P., Maraston, C., Thomas, D., Bender, R., & Colless, M. 2002, ApJ, 579, L13

Sánchez-Blázquez, P., Peletier, R. F., Jiménez-Vicente, J., et al. 2006, MNRAS, 371, 703

Sansom, A. E., de Castro Milone, A., Vazdekis, A., & Sánchez-Blázquez, P. 2013, MNRAS, 435, 952

Strader, J., Brodie, J. P., Cenarro, A. J., Beasley, M. A., & Forbes, D. A. 2005, AJ, 130, 1315

Thomas, D., Maraston, C., & Bender, R. 2003, MNRAS, 339, 897

Usher, C., Forbes, D. A., Brodie, J. P., et al. 2012, MNRAS, 426, 1475

Usher, C., Forbes, D. A., Brodie, J. P., et al. 2015, MNRAS, 446, 369

Usher, C., Forbes, D. A., Spitler, L. R., et al. 2013, MNRAS, 436, 1172

Valdes, F., Gupta, R., Rose, J. A., Singh, H. P., & Bell, D. J. 2004, ApJS, 152, 251

Vasquez, S., Zoccali, M., Hill, V., et al. 2015, arXiv:1507.00425

Vazdekis, A., Cenarro, A. J., Gorgas, J., Cardiel, N., & Peletier, R. F. 2003, MNRAS, 340, 1317

Vazdekis, A., Coelho, P., Cassisi, S., et al. 2015, MNRAS, 449, 1177

Vazdekis, A., Ricciardelli, E., Cenarro, A. J., et al. 2012, MNRAS, 424, 157

Warren, S. R., & Cole, A. A. 2009, MNRAS, 393, 272

West, M. J., Côté, P., Marzke, R. O., & Jordán, A. 2004, Nature, 427, 31

Westera, P., Lejeune, T., Buser, R., Cuisinier, F., & Bruzual, G. 2002, A&A, 381, 524

Woodley, K. A., Harris, W. E., Puzia, T. H., et al. 2010, ApJ, 708, 1335

Worthey, G., Ingermann, B. A., & Serven, J. 2011, ApJ, 729, 148

Yoon, S.-J., Lee, S.-Y., Blakeslee, J. P., et al. 2011, ApJ, 743, 150

Yoon, S.-J., Sohn, S. T., Lee, S.-Y., et al. 2011, ApJ, 743, 149

Yoon, S.-J., Sohn, S. T., Kim, H.-S., et al. 2013, ApJ, 768, 137

Yoon, S.-J., Yi, S. K., & Lee, Y.-W. 2006, Science, 311, 1129

Zhou, X. 1991, A&A, 248, 367
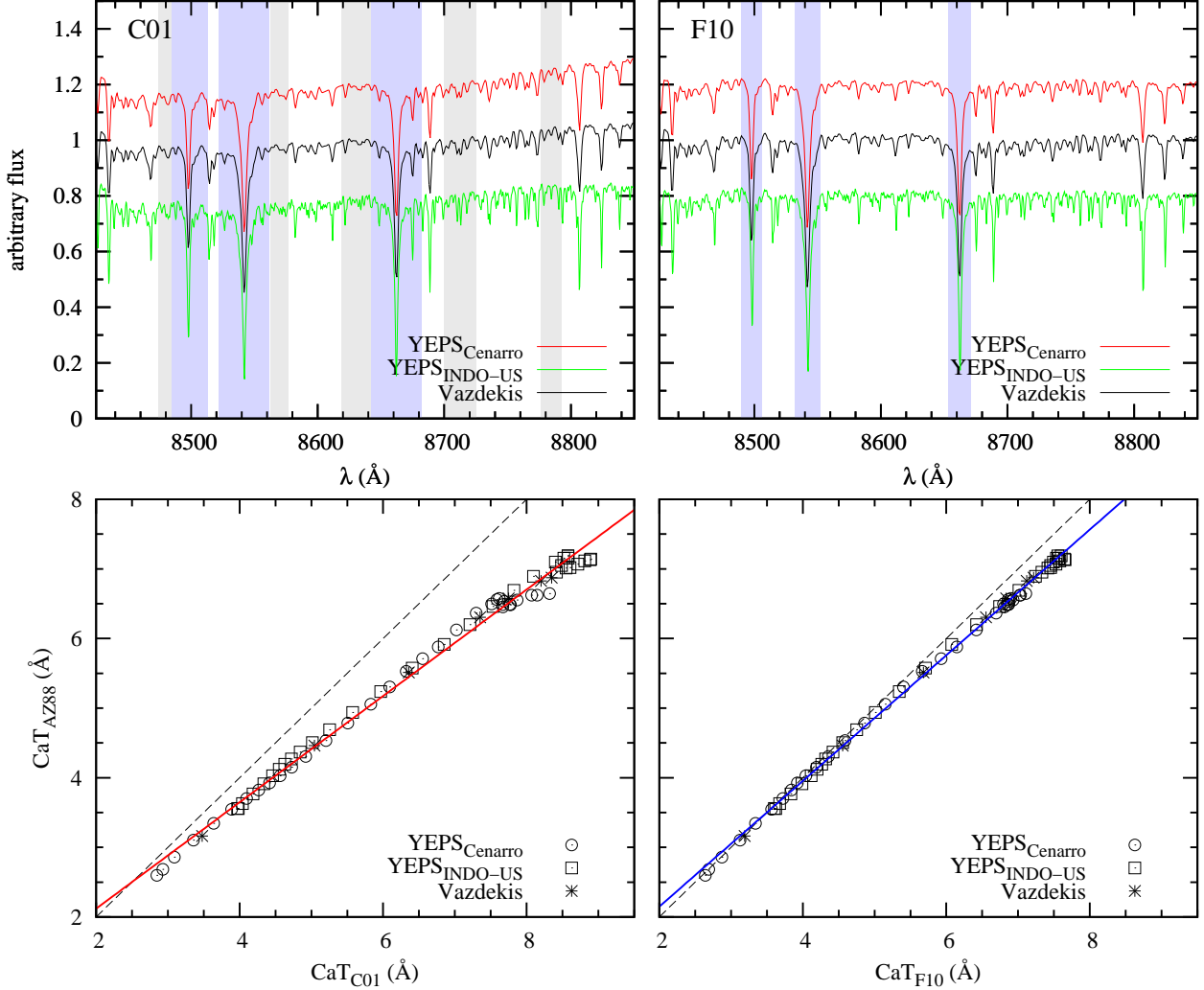
Fig. 1.— (*Upper row*) Examples of model spectra before (*left*) and after fitting (*right*). Red and green lines are YEPS models based on the Cenarro and INDO-US libraries, respectively. Selected models are [Fe/H] = 0.0 at 12 Gyr with [α/Fe] = 0.3. Black lines are the model of Vazdekis et al. (2003) with similar metallicity and age ([Fe/H] = 0.0 and 12.5893 Gyr). The highlighted blue and gray shades in the left panel are, respectively, the CaT index passbands and the continua of the Cenarro definition. The blue shades in the right panel show the CaT index definition used in Armandroff & Zinn (1988) and Foster et al. (2010). (*Bottom row*) Relations between CaT of Armandroff & Zinn (1988), Cenarro et al. (2001a), and Foster et al. (2010). The CaT absorptions are measured from our 13-Gyr models and 12.5893-Gyr models of Vazdekis et al. (2003), simultaneously. Dashed lines are one to one correlation, and red and blue lines are the least-square fit of the data points.
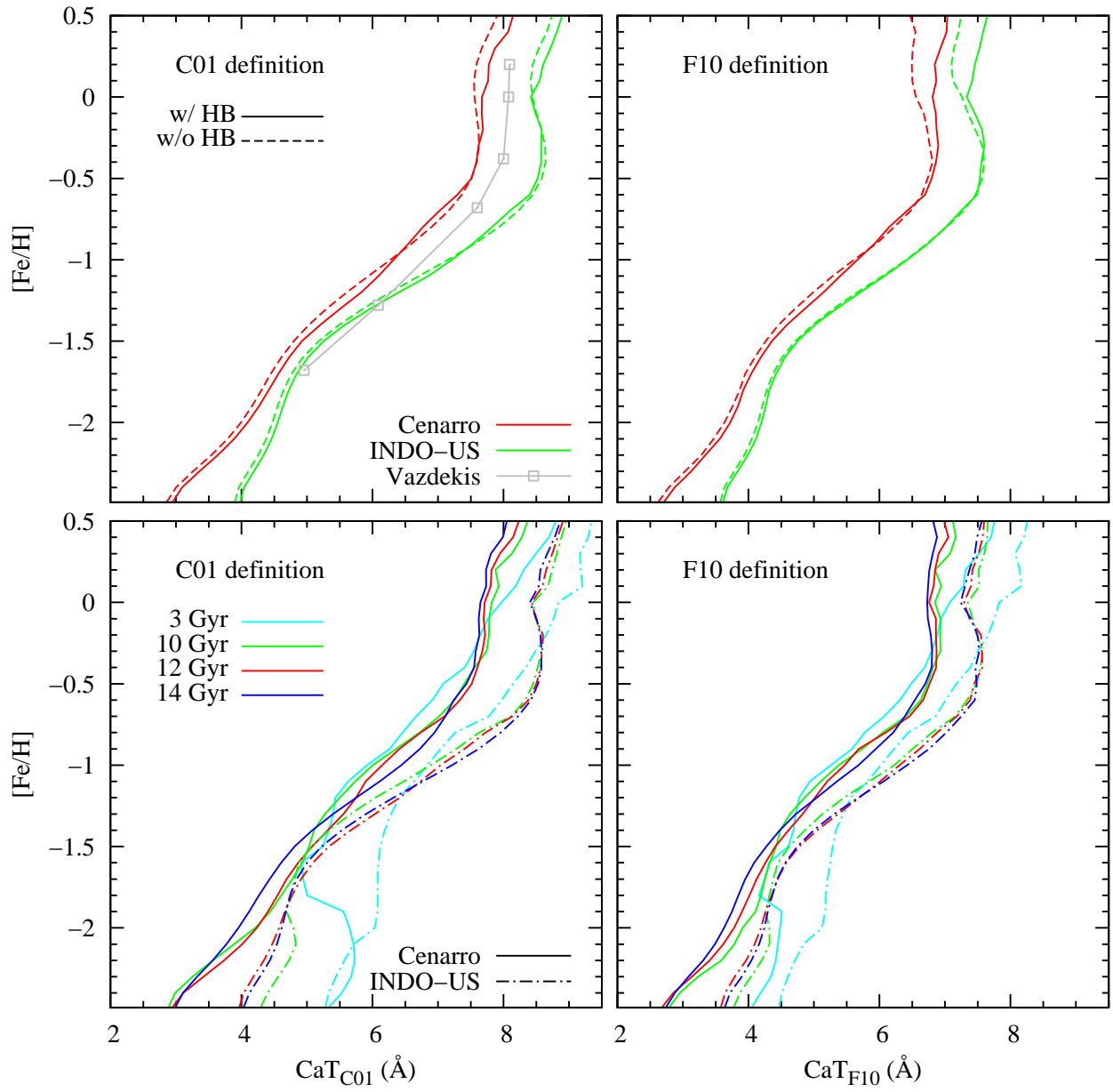
Fig. 2.— The effect of HB stars and age of stellar populations on the simple stellar population model of CaT. The CaT strengths in the left and right panels are measured based on the definitions of Cenarro et al. (2001a) and Foster et al. (2010), respectively. (*Upper*) Red and green solid lines represent the CaT model with HB stars based on the Cenarro and INDO-US, respectively, at the age of 13 Gyr. The dashed lines indicate the CaT model without HB stars. The 12.5893-Gyr model of Vazdekis et al. (2003) is presented as a grey line with points for comparison. Grey points of the Vazdekis et al. (2003) model indicate [Fe/H] = -1.68, -1.28, -0.68, -0.38, 0.00, and 0.20. (*Lower*) Cyan, green, red, and blue lines are models for 3, 10, 12, and 14 Gyr, respectively. Solid and dot dashed lines are models based on the Cenarro and INDO-US library, respectively. The effects of HB stars and age of old stellar population on the CaT model are very small. The CaT definition of F10 strengthens the saturating shape of the CaT–metallicity relations in the metal-rich regime.
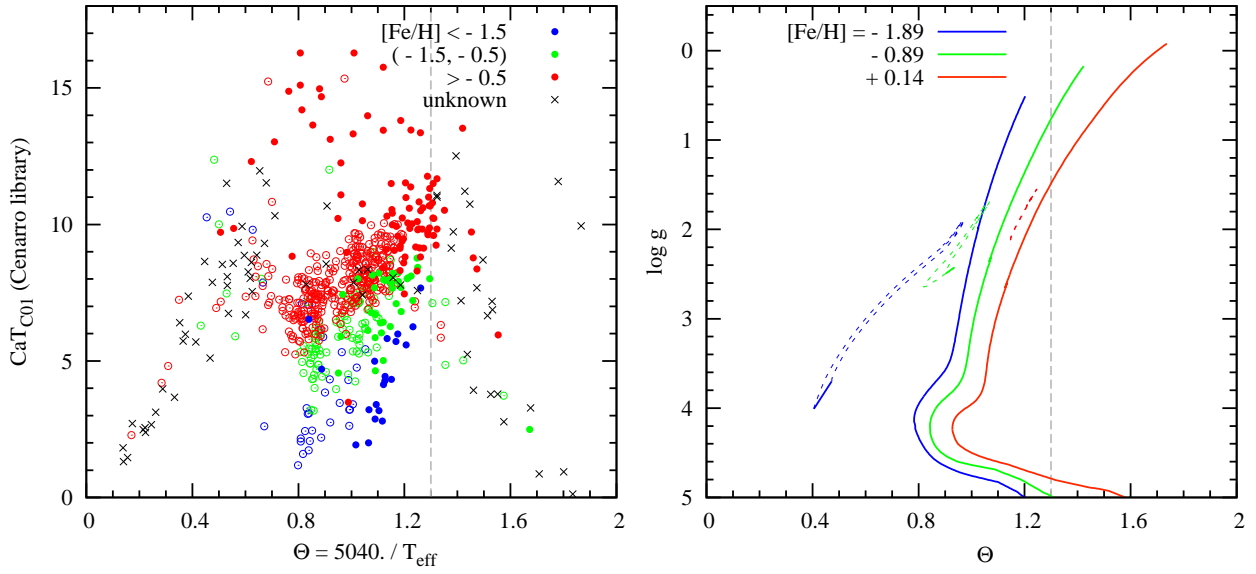
Fig. 3.— (*Left*) The relation between temperature of stars and the strengths of CaT in the Cenarro library. Metallicity of each star is denoted by colors. Open and filled circles indicate dwarf ($\log g \geq 2.0$) and giant (< 2.0) stars, respectively. Stellar library without sufficient information of metallicity or gravity are denoted as black crosses. The vertical dashed grey line indicates $T_{\mathrm{eff}} = 3870$ K. (*Right*) The Y^2-isochrones and HB tracks of 12 Gyr for different metallicities in the temperature and gravity plane. Colors of isochrones correspond to the metallicity bin in the left panel. The dashed grey line also indicates $T_{\mathrm{eff}} = 3870$ K.
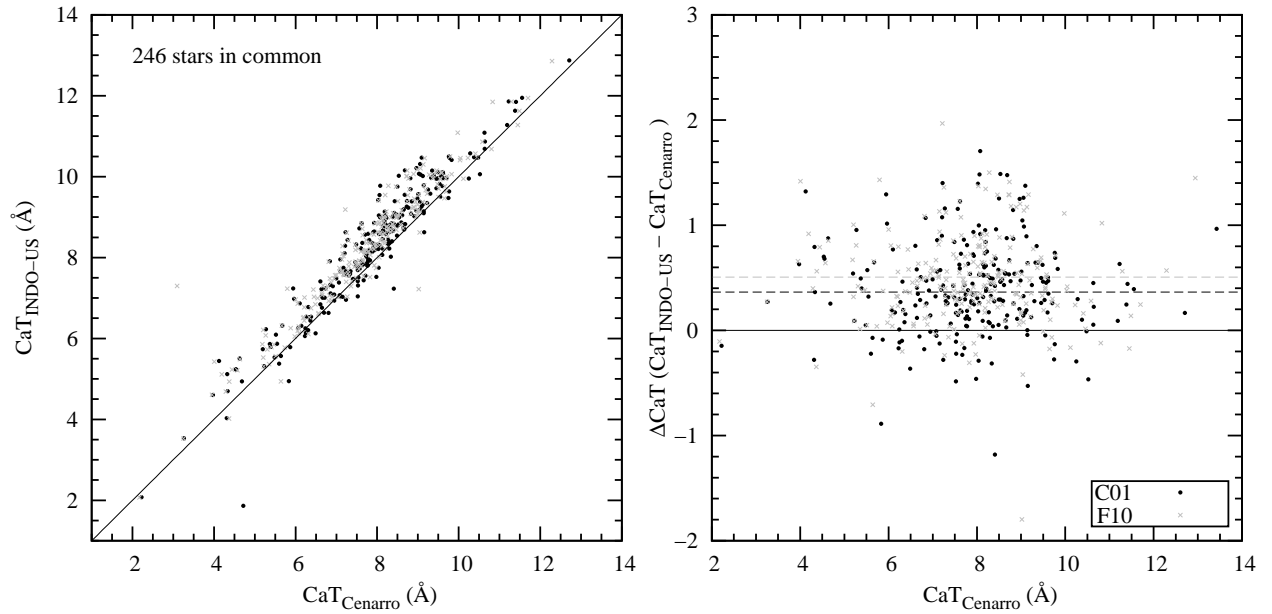
Fig. 4.— The correlation between $CaT_{\mathrm{INDO-US}}$ and CaT_{Cenarro} of stars in common (left) and the deviation of $CaT_{\mathrm{INDO-US}}$ from CaT_{Cenarro} (right). Points are for 246 stars in common in Cenarro and INDO-US libraries. Black and grey points are CaT values which are measured in C01 and F10 definitions. Black lines are the one-to-one relations, and black and grey dashed line in the right panel is the arithmetic average of $CaT_{\mathrm{INDO-US}}$ deviation from CaT_{Cenarro}.
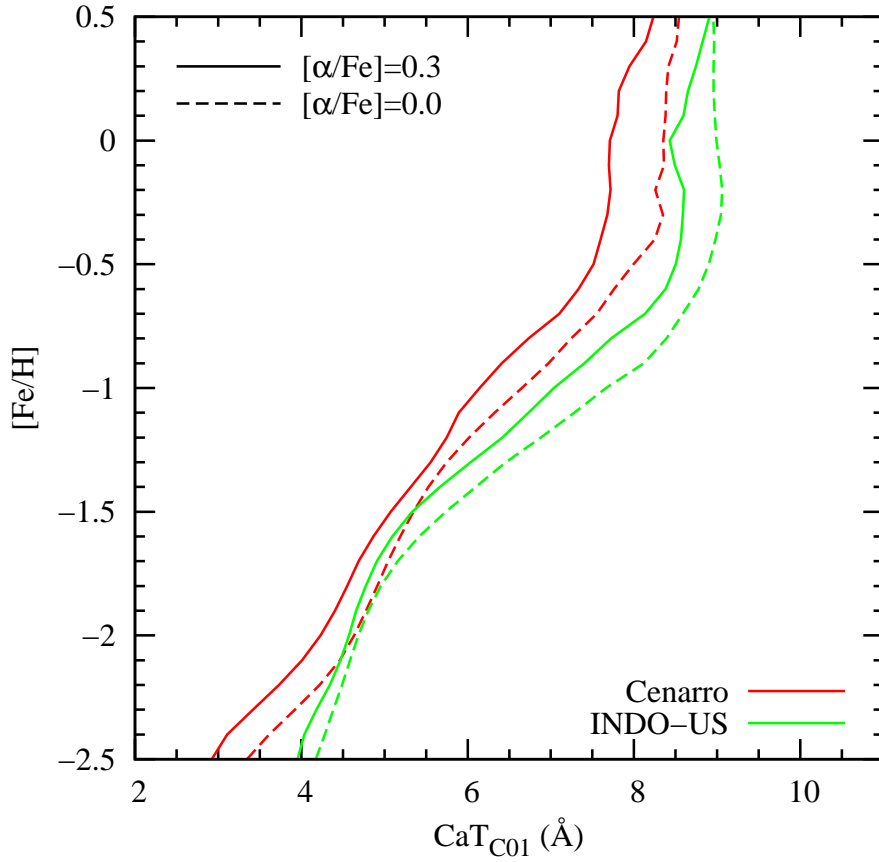
Fig. 5.— The result of CaT models based on the different assumption of α-elements enhancement of empirical stars. Solid and dashed lines are models for $[\alpha/\mathrm{Fe}] = 0.3$ and 0.0 at the age of 12 Gyr. Red and green lines are based on Cenarro and INDO-US library, respectively. Regardless of the $[\alpha/\mathrm{Fe}]$, CaT values do not increase with increasing metallicity in the metal-rich regime.
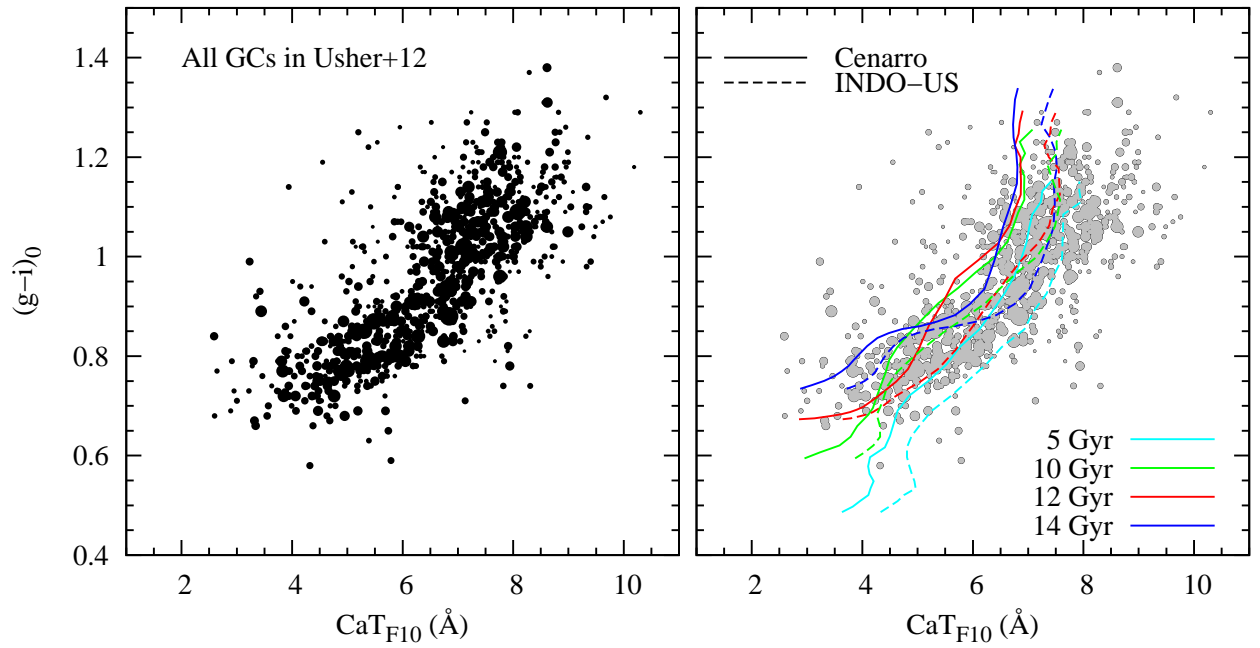
Fig. 6.— The CaT–$(g-i)_0$ relation of 901 GCs (Usher et al. 2012) overlaid with our models. The size of symbols is inversely proportional to the observational error. Cyan, green, red, and blue lines are for 5, 10, 12, and 14 Gyr, respectively. Solid and dashed lines are the models based on Cenarro and INDO-US libraries, respectively. The CaT–$(g-i)_0$ relations are nonlinear both for observed and modeled GCs.
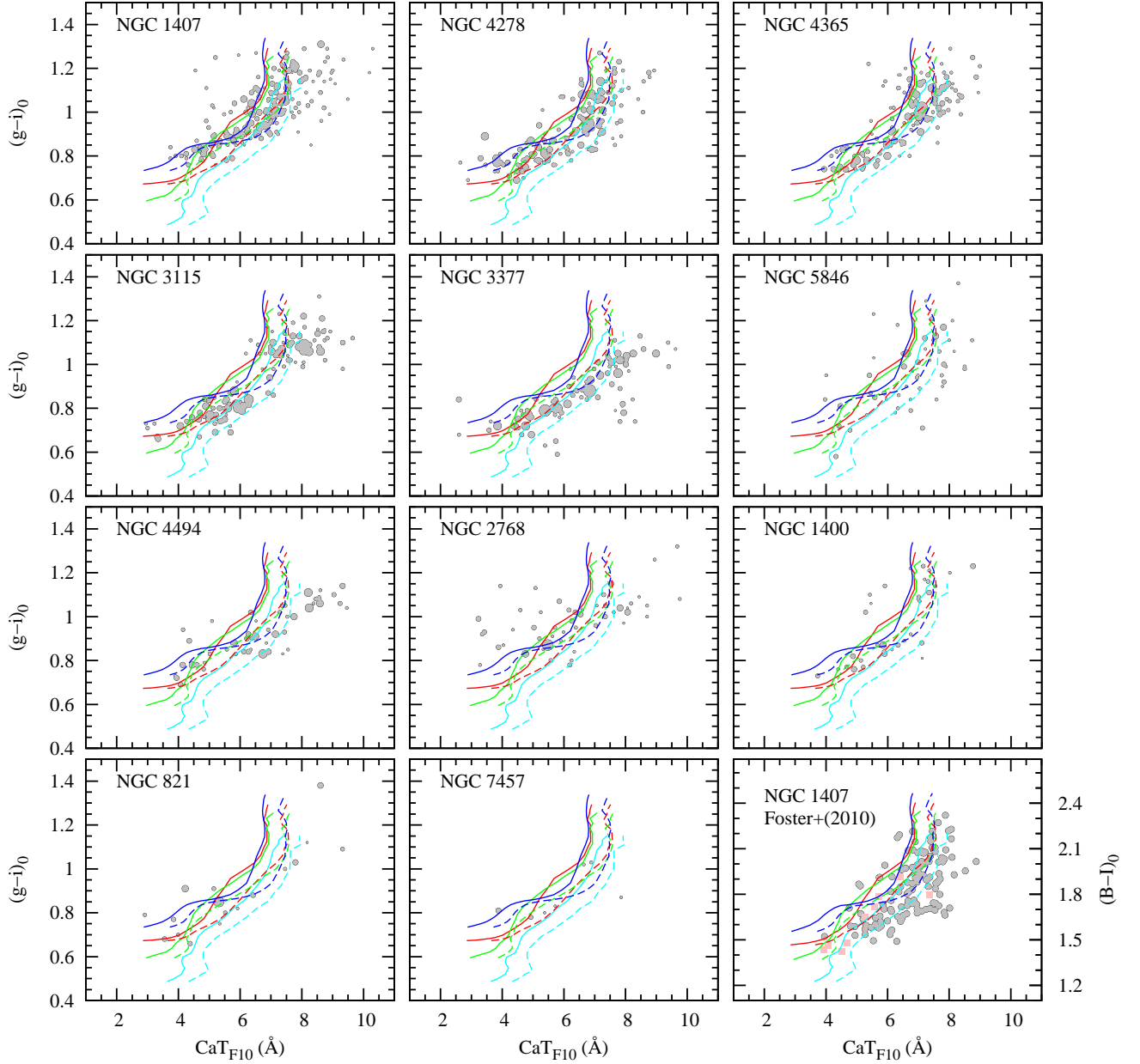
Fig. 7.— Same as Figure 6 but for GCs in individual galaxies. The GCs in rightmost bottom panel is from Foster et al. (2010), and gray circles and red squares are GCs in NGC 1407 and the MW, respectively. The size of symbols in this panel is inversely proportional to the observational error given in Foster et al. (2010).
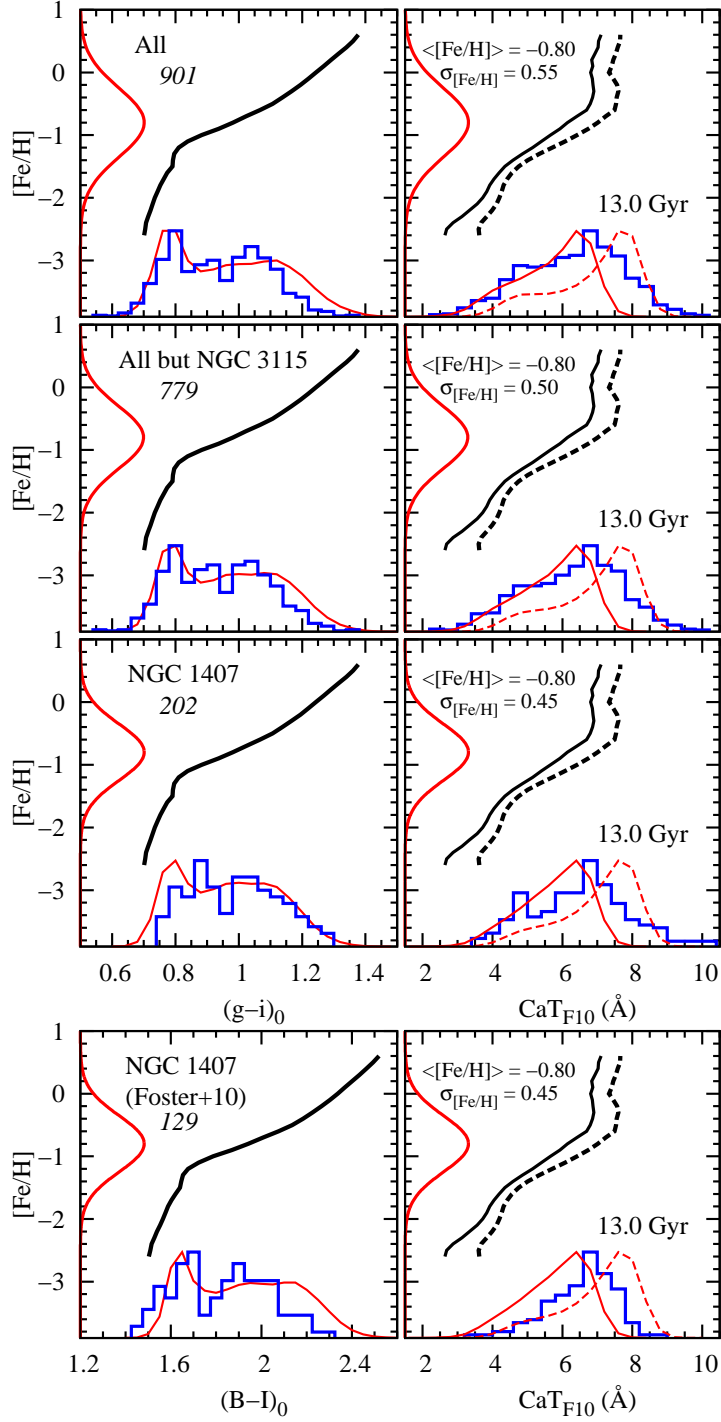
Fig. 8.— The effect of the nonlinear nature of CaT–metallicity and color–metallicity relations on the projection of unimodal MDFs. The observed distribution (blue and open histograms) of GCs in ETGs are from Usher et al. (2012) and Foster et al. (2010). The black lines in each plot are the adopted CMRs and IMRs, and the black solid and dashed lines in the right panels are models based on Cenarro and INDO-US libraries, respectively. The single Gaussian MDFs of 10^6 model GCs are assumed, and the best-fit age, mean metallicity and standard deviation of [Fe/H] of each Gaussian MDF to reproduce the distributions of $(g - i)_0$, $(B - I)_0$, and CaT_{F10} simultaneously are indicated. The red solid and dashed lines in the bottom of each plot show the result of the unimodal MDF projection to $(g - i)_0$, $(B - I)_0$, and CaT_{F10}. Our models reproduce the overall shapes of both CaT and color distributions of GCs simultaneously.
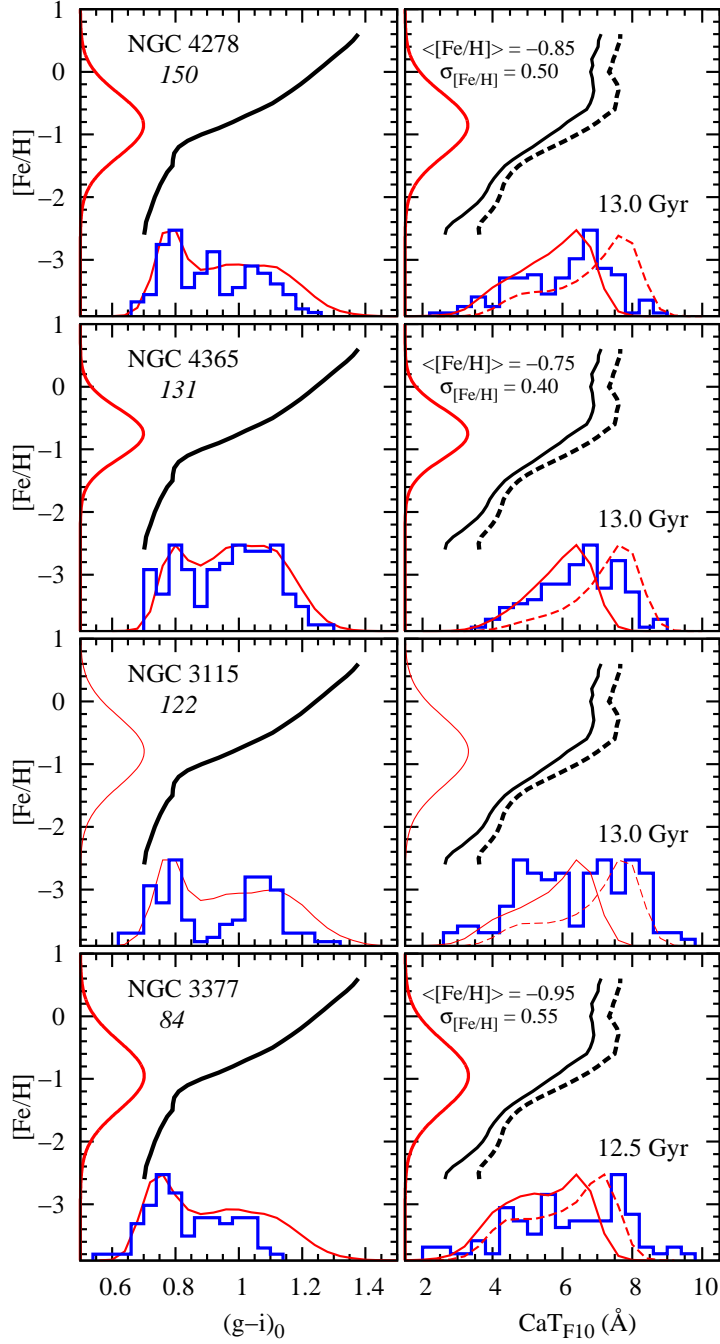
Fig. 9.— Same as Figure 8 but for NGC 4278, NGC 4365, NGC 3115, and NGC 3377. Our single Gaussian projection test is hard to reproduce $(g - i)_0$ and CaT distributions of GCs in NGC 3115 at the same time.
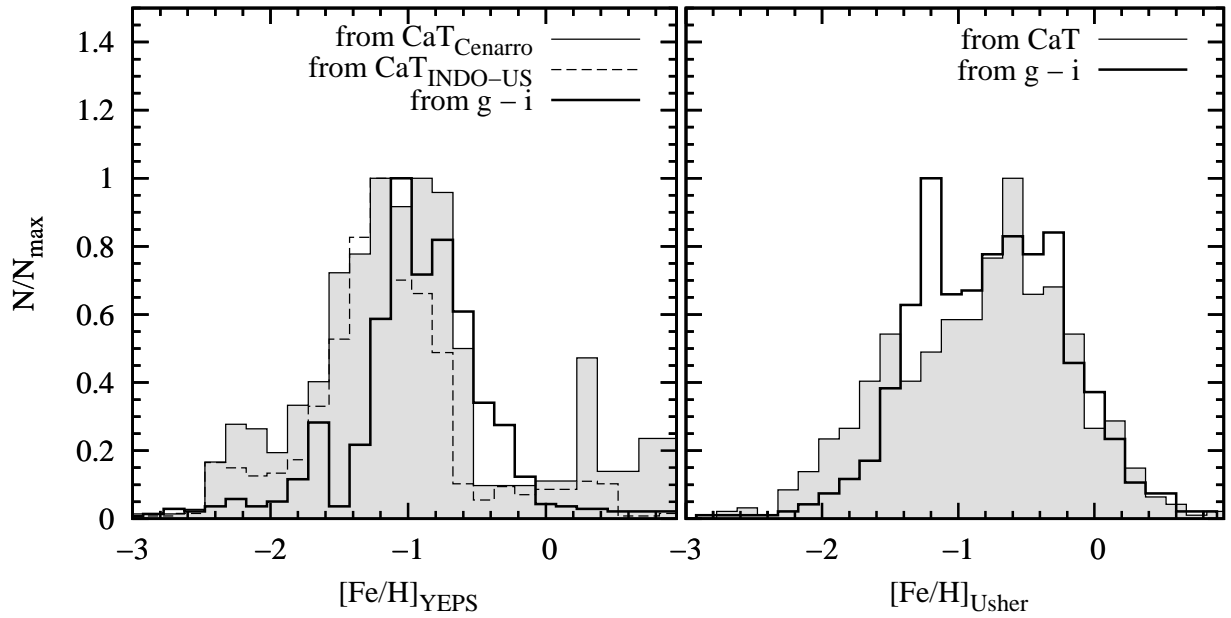
Fig. 10.— The comparison of derived GC MDFs based on different CaT–metallicity and $(g-i)_0$–metallicity relations. The left panel is the GC MDFs derived from our relations, and the right panel is from Usher et al. (2012). Grey and empty histograms are derived GC MDFs from CaT and $(g-i)_0$ color of 779 GCs, respectively.

Table 1. CaT of YEPS simple stellar population models for [α/Fe]=0.3 (based on empirical spectra of Cenarro and INDO-US library).

| [Fe/H]	$t = 3.0$ (Gyr)		5.0		10.0		12.0		14.0	
	CaT_{C01}	CaT_{F10}	CaT_{C01}	CaT_{F10}	CaT_{C01}	CaT_{F10}	CaT_{C01}	CaT_{F10}	CaT_{C01}	CaT_{F10}
					Cenarro library					
-2.5	5.30	4.03	4.10	3.51	2.87	2.76	2.92	2.65	2.97	2.72
-2.4	5.52	4.18	4.33	3.62	2.98	2.95	3.10	2.85	3.10	2.87
-2.3	5.67	4.34	4.52	3.82	3.25	3.23	3.42	3.13	3.32	3.08
-2.2	5.72	4.41	4.66	3.95	3.56	3.58	3.73	3.40	3.55	3.30
-2.1	5.70	4.44	4.77	4.10	3.88	3.78	4.00	3.61	3.76	3.48
-2.0	5.64	4.48	4.84	4.14	4.21	3.91	4.23	3.78	3.95	3.62
-1.9	5.55	4.51	4.90	4.20	4.43	4.10	4.40	3.90	4.11	3.74
-1.8	5.00	4.15	4.64	4.13	4.60	4.19	4.54	4.01	4.26	3.84
-1.7	4.94	4.24	4.53	4.10	4.77	4.24	4.68	4.12	4.42	3.95
-1.6	4.91	4.31	4.59	4.13	4.92	4.32	4.86	4.25	4.60	4.08
-1.5	5.24	4.60	4.95	4.40	5.03	4.42	5.07	4.41	4.81	4.27
-1.4	5.33	4.68	5.09	4.50	5.10	4.48	5.31	4.61	5.07	4.47
-1.3	5.39	4.71	5.19	4.56	5.27	4.63	5.55	4.82	5.39	4.72
-1.2	5.43	4.77	5.27	4.63	5.49	4.85	5.74	5.01	5.75	5.04
-1.1	5.62	4.93	5.48	4.84	5.73	5.10	5.89	5.20	6.10	5.34
-1.0	5.91	5.25	5.91	5.20	6.00	5.37	6.14	5.46	6.43	5.67
-0.9	6.26	5.57	6.16	5.52	6.35	5.73	6.40	5.68	6.72	5.94
-0.8	6.45	5.77	6.40	5.76	6.71	6.05	6.73	6.09	6.94	6.21
-0.7	6.66	6.06	6.68	6.11	7.01	6.40	7.10	6.45	7.11	6.38
-0.6	6.91	6.31	6.94	6.35	7.25	6.62	7.33	6.66	7.24	6.53
-0.5	7.07	6.48	7.15	6.57	7.40	6.73	7.51	6.76	7.43	6.69
-0.4	7.40	6.68	7.47	6.75	7.55	6.81	7.59	6.86	7.55	6.79
-0.3	7.54	6.79	7.68	6.87	7.74	6.92	7.67	6.87	7.57	6.80
-0.2	7.63	6.88	7.83	6.97	7.77	6.92	7.71	6.86	7.63	6.78
-0.1	7.76	6.93	7.93	7.01	7.78	6.93	7.69	6.86	7.62	6.73
0.0	7.96	7.07	8.10	7.07	7.82	6.84	7.71	6.75	7.64	6.72
0.1	8.18	7.28	8.32	7.23	7.92	6.94	7.80	6.82	7.73	6.74
0.2	8.30	7.31	8.32	7.25	7.87	6.84	7.81	6.84	7.73	6.76
0.3	8.49	7.51	8.45	7.41	8.12	7.07	7.94	6.90	7.80	6.81
0.4	8.69	7.70	8.56	7.49	8.27	7.16	8.14	7.04	7.98	6.87
0.5	8.79	7.75	8.66	7.58	8.36	7.12	8.23	6.98	8.05	6.81
					INDO-US library					
-2.5	5.27	4.46	4.93	4.23	4.28	3.76	3.95	3.56	4.02	3.62
-2.4	5.32	4.51	5.04	4.33	4.39	3.86	4.03	3.64	4.12	3.71
-2.3	5.44	4.60	5.24	4.48	4.56	4.03	4.18	3.79	4.28	3.89
-2.2	5.56	4.70	5.42	4.63	4.72	4.20	4.34	3.96	4.43	4.04
-2.1	5.71	4.83	5.53	4.75	4.82	4.32	4.46	4.09	4.54	4.16
-2.0	6.03	5.12	5.76	4.96	4.79	4.31	4.57	4.19	4.61	4.24
-1.9	6.07	5.17	5.70	4.94	4.68	4.26	4.65	4.26	4.67	4.29
-1.8	6.07	5.17	5.59	4.89	4.73	4.31	4.77	4.35	4.74	4.36
-1.7	6.07	5.20	5.49	4.85	4.81	4.38	4.90	4.44	4.84	4.43
-1.6	6.08	5.24	5.42	4.80	4.87	4.44	5.09	4.57	4.99	4.56
-1.5	6.11	5.28	5.41	4.80	5.06	4.62	5.33	4.77	5.22	4.74

Table 1—Continued

[Fe/H]	$t = 3.0$ (Gyr)		5.0		10.0		12.0		14.0	
	$CaT_{\rm C01}$	$CaT_{\rm F10}$	$CaT_{\rm C01}$	$CaT_{\rm F10}$	$CaT_{\rm C01}$	$CaT_{\rm F10}$	$CaT_{\rm C01}$	$CaT_{\rm F10}$	$CaT_{\rm C01}$	$CaT_{\rm F10}$
-1.4	6.18	5.33	5.49	4.88	5.33	4.85	5.66	5.04	5.52	4.99
-1.3	6.28	5.44	5.64	5.05	5.66	5.12	6.03	5.36	5.89	5.30
-1.2	6.40	5.55	5.87	5.26	6.04	5.45	6.41	5.69	6.32	5.67
-1.1	6.63	5.81	6.22	5.60	6.47	5.84	6.73	6.00	6.76	6.06
-1.0	6.82	6.01	6.57	5.92	6.88	6.22	7.03	6.30	7.21	6.42
-0.9	7.03	6.22	6.93	6.23	7.27	6.50	7.40	6.61	7.61	6.75
-0.8	7.26	6.43	7.30	6.52	7.62	6.80	7.72	6.87	7.95	7.02
-0.7	7.77	6.85	7.88	6.92	8.11	7.15	8.13	7.18	8.22	7.24
-0.6	7.97	7.00	8.14	7.10	8.33	7.33	8.37	7.38	8.42	7.45
-0.5	8.14	7.17	8.31	7.33	8.45	7.48	8.50	7.44	8.52	7.48
-0.4	8.34	7.38	8.45	7.46	8.52	7.53	8.56	7.57	8.57	7.46
-0.3	8.48	7.50	8.59	7.61	8.58	7.57	8.58	7.56	8.57	7.52
-0.2	8.64	7.65	8.61	7.62	8.55	7.48	8.60	7.55	8.56	7.49
-0.1	8.76	7.75	8.61	7.62	8.49	7.41	8.49	7.37	8.50	7.39
0.0	8.83	7.82	8.61	7.63	8.45	7.34	8.43	7.29	8.40	7.23
0.1	9.20	8.16	9.04	7.95	8.67	7.52	8.59	7.39	8.53	7.30
0.2	9.17	8.14	9.02	7.92	8.74	7.51	8.64	7.41	8.56	7.37
0.3	9.16	8.07	9.05	7.92	8.81	7.60	8.74	7.51	8.66	7.45
0.4	9.29	8.20	9.14	7.98	8.88	7.64	8.82	7.57	8.78	7.48
0.5	9.34	8.25	9.20	8.03	8.95	7.65	8.90	7.59	8.86	7.56

Table 2. GMM (Muratov & Gnedin 2010) analysis for distributions of Figures 8 and 9.

All GCs	μ_1	σ_1	p_1	μ_2	σ_2	p_2	$P(\chi^2)$	$P(DD)$	$P(kurt)$
$CaT_{\text{Usher et al. (2012)}}$	5.087	0.9359	0.3428	7.239	0.9749	0.6572	< 0.001	0.184	0.001
$CaT_{\text{Model (Cenarro)}}$	5.224	0.9263	0.5325	6.704	0.4628	0.4675	< 0.010	0.010	< 0.010
$CaT_{\text{Model (INDO−US)}}$	5.994	1.0240	0.4103	7.902	0.4990	0.5897	< 0.010	0.040	< 0.010
$(g-i)_{\text{Usher et al. (2012)}}$	0.812	0.0688	0.3967	1.051	0.1045	0.6033	< 0.001	0.115	< 0.001
$(g-i)_{\text{Model}}$	0.802	0.0461	0.3110	1.071	0.1391	0.6890	< 0.010	0.010	< 0.010
All but NGC 3115	μ_1	σ_1	p_1	μ_2	σ_2	p_2	$P(\chi^2)$	$P(DD)$	$P(kurt)$
$CaT_{\text{Usher et al. (2012)}}$	4.868	0.8437	0.2713	7.090	1.0084	0.7287	< 0.001	0.175	0.009
$CaT_{\text{Model (Cenarro)}}$	5.329	0.9002	0.5332	6.689	0.4650	0.4668	< 0.010	0.030	< 0.010
$CaT_{\text{Model (INDO−US)}}$	6.076	1.0035	0.3807	7.877	0.5202	0.6193	< 0.010	0.210	0.030
$(g-i)_{\text{Usher et al. (2012)}}$	0.817	0.0700	0.3701	1.041	0.1115	0.6299	< 0.001	0.145	< 0.001
$(g-i)_{\text{Model}}$	0.806	0.0461	0.3038	1.064	0.1299	0.6962	< 0.010	< 0.010	< 0.010
NGC 1407	μ_1	σ_1	p_1	μ_2	σ_2	p_2	$P(\chi^2)$	$P(DD)$	$P(kurt)$
$CaT_{\text{Usher et al. (2012)}}$	4.848	0.4991	0.1575	6.995	1.1276	0.8425	0.054	0.279	0.119
$CaT_{\text{Foster et al. (2010)}}$	5.959	0.7592	0.3757	7.235	0.5688	0.6243	0.050	0.600	0.556
$CaT_{\text{Model (Cenarro)}}$	5.360	0.8525	0.5231	6.644	0.4737	0.4769	< 0.010	0.010	< 0.010
$CaT_{\text{Model (INDO−US)}}$	6.216	0.9859	0.3947	7.869	0.5116	0.6053	< 0.010	0.160	0.490
$(g-i)_{\text{Usher et al. (2012)}}$	0.864	0.0540	0.3329	1.076	0.1090	0.6671	< 0.001	0.297	< 0.001
$(g-i)_{\text{Model}}$	0.808	0.0429	0.2723	1.047	0.1255	0.7277	< 0.010	0.010	< 0.010
$(B-I)_{\text{Foster et al. (2010)}}$	1.650	0.0812	0.3761	1.973	0.1441	0.6239	0.001	0.248	< 0.001
$(B-I)_{\text{Model}}$	1.669	0.0546	0.2625	2.038	0.1892	0.7375	< 0.010	< 0.010	< 0.010
NGC 4278	μ_1	σ_1	p_1	μ_2	σ_2	p_2	$P(\chi^2)$	$P(DD)$	$P(kurt)$
$CaT_{\text{Usher et al. (2012)}}$	4.939	0.9225	0.4074	7.097	0.6919	0.5926	< 0.001	0.266	0.130
$CaT_{\text{Model (Cenarro)}}$	5.223	0.9005	0.5763	6.688	0.4535	0.4237	< 0.010	< 0.010	< 0.010
$CaT_{\text{Model (INDO−US)}}$	5.989	0.9944	0.4409	7.883	0.5070	0.5591	< 0.010	0.020	< 0.010
$(g-i)_{\text{Usher et al. (2012)}}$	0.796	0.0497	0.3766	1.014	0.1108	0.6234	< 0.001	0.299	< 0.001
$(g-i)_{\text{Model}}$	0.824	0.0495	0.4372	1.080	0.1088	0.5628	< 0.010	0.010	< 0.010
NGC 4365	μ_1	σ_1	p_1	μ_2	σ_2	p_2	$P(\chi^2)$	$P(DD)$	$P(kurt)$
$CaT_{\text{Usher et al. (2012)}}$	4.945	0.5368	0.1786	7.026	0.8675	0.8214	0.046	0.201	0.069
$CaT_{\text{Model (Cenarro)}}$	5.593	0.8056	0.5228	6.691	0.4405	0.4772	< 0.010	0.010	0.040
$CaT_{\text{Model (INDO−US)}}$	6.538	0.9549	0.3763	7.913	0.4874	0.6237	< 0.010	0.300	1.000
$(g-i)_{\text{Usher et al. (2012)}}$	0.796	0.0440	0.2755	1.048	0.0972	0.7245	< 0.001	0.122	< 0.001
$(g-i)_{\text{Model}}$	0.820	0.0446	0.2322	1.055	0.1162	0.7678	< 0.010	< 0.010	< 0.010
NGC 3115	μ_1	σ_1	p_1	μ_2	σ_2	p_2	$P(\chi^2)$	$P(DD)$	$P(kurt)$
$CaT_{\text{Usher et al. (2012)}}$	5.551	1.0878	0.5711	7.983	0.6911	0.4289	0.002	0.262	0.018
$(g-i)_{\text{Usher et al. (2012)}}$	0.785	0.0576	0.4727	1.087	0.0694	0.5273	< 0.001	0.024	< 0.001
NGC 3377	μ_1	σ_1	p_1	μ_2	σ_2	p_2	$P(\chi^2)$	$P(DD)$	$P(kurt)$
$CaT_{\text{Usher et al. (2012)}}$	5.341	1.1644	0.5560	7.794	0.7629	0.4440	0.085	0.432	0.098
$CaT_{\text{Model (Cenarro)}}$	5.056	0.9288	0.6596	6.690	0.4434	0.3404	< 0.010	0.010	< 0.010
$CaT_{\text{Model (INDO−US)}}$	5.302	0.8913	0.5060	7.235	0.5057	0.4940	< 0.010	< 0.010	< 0.010
$(g-i)_{\text{Usher et al. (2012)}}$	0.788	0.0793	0.6642	1.013	0.0556	0.3358	0.006	0.154	0.007
$(g-i)_{\text{Model}}$	0.772	0.0523	0.3615	1.031	0.1384	0.6385	< 0.010	< 0.010	< 0.010

Note. — The mean, standard deviation, and portion of two groups analyzed by the GMM test are expressed as $\mu_{1,2}$, $\sigma_{1,2}$, and $p_{1,2}$, respectively. The statistical significance of bimodality are expressed as P-values in the last three columns. If P is less than 0.05, the GMM test strongly suggests the bimodality of a distribution.